Impurities in 4H silicon carbide: Site preference, lattice distortion, solubility, and charge transition levels

Yuanchao Huang,[1,2] ⓘ Rong Wang,[2] ⓘ Deren Yang,[1,2] ⓘ and Xiaodong Pi[1,2,a)] ⓘ

AFFILIATIONS

[1]State Key Laboratory of Silicon and Advanced Semiconductor Materials & School of Materials Science and Engineering, Zhejiang University, Hangzhou, Zhejiang 310027, China
[2]Institute of Advanced Semiconductors & Zhejiang Provincial Key Laboratory of Power Semiconductor Materials and Devices, Hangzhou Global Scientific and Technological Innovation Center, Zhejiang University, Hangzhou, Zhejiang 311215, China

Note: This paper is part of the special topic, Defects in Semiconductors 2024.
[a)]Author to whom correspondence should be addressed: xdpi@zju.edu.cn

ABSTRACT

4H Silicon carbide (SiC) is widely recognized as one of the most advanced wide bandgap semiconductors used in the production of high-efficiency power electronic devices. Impurities play a crucial role in achieving the desired electrical properties in 4H-SiC, yet the understanding of impurities in this material remains limited. In this study, first-principles formation-energy calculations were employed to establish a comprehensive database of formation-energy diagrams for impurities in 4H-SiC. This database includes valuable information on site preference, lattice distortion, solubility, and charge transition levels (CTLs) of the impurities. The site preference for each impurity is closely related to factors such as the Fermi energy, chemical potential, and the impurity species itself. To assess the lattice distortion caused by each impurity, a comparison was made between the volume changes before and after doping. Moreover, the solubility of each impurity was determined using the detailed balance theory, thereby enabling a direct measure of the maximum impurity concentration achievable in the material. Based on the CTLs, the impurities in 4H-SiC were classified into four categories: *n*-type impurities, *p*-type impurities, amphoteric impurities, and non-electroactive impurities. This comprehensive property database for impurities in 4H-SiC provides valuable insights for tailoring the material properties through controlled doping, thereby ultimately leading to enhanced performance of power electronic devices.

I. INTRODUCTION

Impurities play a pivotal role in shaping the electrical, optical, and mechanical characteristics of 4H silicon carbide (SiC).[1–3] Various attributes, including site preference, lattice distortion, solubility, and charge transition levels (CTLs), offer insights into the nature of these impurities.[4–11] Site preference delineates the distinct positions impurities assume within the SiC crystal lattice, dictated by their size and electronic configuration. Typically, impurities may reside in Si or C lattice sites or occupy interstitial positions. The introduction of impurities induces lattice distortions, stemming from disparities in size and electronic properties between the

impurity and host atoms. These distortions have far-reaching effects on the electronic band structure, phonon dispersion, and overall properties of SiC. Solubility, a critical factor, denotes the maximum concentration of impurities that can be seamlessly incorporated into the lattice without precipitate formation or other defect structures. Influenced by variables such as temperature, impurity size, and defect formation energy, solubility in SiC is a dynamic parameter that shapes the material's characteristics. Impurities introduce energy levels within SiC's bandgap, acting as electron traps or recombination centers. These energy levels, known as charge transition levels (CTLs), significantly influence

the electronic properties of SiC.[8–11] Understanding these intricate interplays between impurities and SiC properties is paramount for advancing the knowledge base in semiconductor materials and optimizing SiC-based devices.

Impurities, such as nitrogen (N) and phosphorus (P), are commonly used as *n*-type impurities in 4H-SiC.[12–16] N has a relatively low ionization energy (0.06 eV), making it an effective donor for generating additional electrons in the conduction band.[1,3,15] The solubility of N in 4H-SiC during physical vapor transport (PVT) growth at ~2200 °C is approximately 1.5×10^{19} cm^{-3}.[13,14] P, with a similar ionization energy to N, is also an effective *n*-type impurity.[9,15] The solubility of P in 4H-SiC is higher than that of N, resulting in better activation of P$^+$ implantation compared to N$^+$ implantation.[15] For *p*-type doping, aluminum (Al) is the primary impurity used in 4H-SiC.[17–21] It has an ionization energy of approximately 0.23 eV and acts as an acceptor impurity.[17–20] The highest achieved doping concentration for Al in 4H-SiC is 1.1×10^{21} cm^{-3} through epitaxial growth at 2300 °C.[21] Boron (B) is also a *p*-type impurity, but its use for intentional *p*-type doping is limited due to its anomalous diffusion behavior.[22–27] B can substitute for both Si and C sites, with ionization energies of approximately 0.58 eV for B$_{Si}$ and 0.30 eV for B$_C$.[22] Vanadium (V) is an amphoteric impurity used for the growth of semi-insulating 4H-SiC, which requires high resistivity for radio-frequency devices.[28–30] V creates deep energy levels in the bandgap that can accept both electrons and holes. The CTLs of V are $\epsilon(0/1+)$ at $E_V + 0.97$ eV and $\epsilon(0/1-)$ at $E_V + 1.97$ eV.[28,29] The solubility of V during PVT growth of 4H-SiC at 2100–2300 °C is approximately 3.0–4.0×10^{17} cm^{-3}.[30] Hydrogen (H) is also an amphoteric impurity that can compensate for impurities in 4H-SiC. In *n*-type 4H-SiC, H compensation can pin the Fermi energy and hinder the increase of electron concentration in highly N-doped 4H-SiC. In *p*-type 4H-SiC, H compensation is generally negligible compared to V_C compensation.[31] Germanium (Ge) and tin (Sn) can be incorporated on substitutional Si sites in 4H-SiC without creating new energy levels in the bandgap.[32,33] The specific doping solubilities of Ge and Sn in 4H-SiC are not provided in the supplementary material. Additionally, the CTLs of titanium (Ti), chromium (Cr), and molybdenum (Mn) in 4H-SiC have been reported,[34–37] but their solubilities are not mentioned. Thus far, the understanding of 4H-SiC remains incomplete.

First-principles calculations play a pivotal role in the examination of defects and impurities within semiconductor materials, furnishing intricate details at the atomic scale and facilitating a profound comprehension of the material's electronic structure and band characteristics.[7–11] Notably, extensive density functional theory (DFT)-based defect calculations have explored a diverse spectrum of defects and impurities in SiC, ranging from vacancies and interstitials to intricate dopant interactions.[38–42] These studies have provided detailed insights into the energetics and electronic properties, contributing significantly to the wealth of knowledge in this field. However, it is important to note that, to date, a comprehensive database specifically focusing on DFT-based defect calculations for impurities in SiC is lacking. Addressing this gap, our work introduces an automated first-principles formation-energy calculations code designed to establish a thorough database of formation-energy diagrams for impurities in 4H-SiC.

Encompassing a broad array of impurities from the periodic table, excluding radioactive elements, rare earth elements, and VIIIA group elements, this database serves as a valuable resource. The database allows for the exploration of several critical aspects of impurities in 4H-SiC, including site preference, lattice distortion, solubility, and CTLs (charge transition levels). By providing a comprehensive and organized dataset, our developed database offers essential information for researchers and engineers engaged in SiC-based device design, optimization, and material characterization. This resource aims to enhance the efficacy of future investigations and applications in SiC materials science by filling the existing gap in DFT-based defect calculations for impurities in SiC.

II. COMPUTATIONAL METHODS

First-principles calculations are performed using the projector-augmented wave (PAW) method implanted in the Vienna *ab initio* simulation package (VASP).[43] The wave functions are expanded by using the plane wave energy cutoff of 500 eV. The Perdew–Burke–Ernzerhof (PBE) functional with the generalized gradient approximation (GGA) exchange correlation is employed to describe the exchange-correlation interactions.[44,45] The screened hybrid density functional of Heyd, Scuseria, and Ernzerhof (HSE06) is adopted to calculate the electronic properties and the accurate geometries and energetics.[46,47] Impurities in 4H-SiC are modeled in a $4 \times 4 \times 1$ supercell of 4H-SiC with 128 atoms. Brillouin-zone integrations are approximated by using special k-point sampling of the Monkhorst–Pack scheme with a k-point mesh of $2 \times 2 \times 2$. The structural optimizations are performed by the PBE exchange-correlation functional. During structural optimization, atomic positions are fully relaxed until the total energy per cell and the force on each atom converge to less than 1×10^{-6} and 0.01 eV/Å, respectively. In order to gain accurate bandgap energies and thus correct defect level positions, the screened hybrid functional of HSE06 is employed.[17–19] The spin-polarized calculations are considered. The calculated lattice parameters of 4H-SiC are $a = 3.07$ Å and $c = 10.05$ Å. The calculated bandgap energy of 4H-SiC is 3.18 eV, which agrees well with experimental results.[1]

An automated first-principles formation-energy calculations code is developed in this work. The formation energy of a impurity α at the charge state q in 4H-SiC is calculated by using[7]

$$\Delta H_f(\alpha, q) = \Delta H_f(\alpha, 0) - q\varepsilon(0/q) + qE_F, \quad (1)$$

where $\Delta H_f(\alpha, 0) = E_{tot}(\alpha, 0) + E_{tot}(\text{host}) + \sum n_i\mu_i$. $E_{tot}(\alpha, 0)$ is the total energy of the host supercell containing the impurity α; $E_{tot}(\text{host})$ (host) is the total energy of the host supercell; n_i is the number of atoms removed from or added into the supercell; μ_i is the chemical potential of constituent i referred to elemental solid or gas. $\varepsilon(0/q)$ is the charge-state transition levels; E_F is the Fermi energy referred to the valence band maximum (VBM) of the host. Four steps are needed to obtain $\Delta H_f(\alpha, q)$. The schematic workflow is shown in Fig. 1. For step 1, it is the generation and relaxation of substitutional and interstitial configurations with impurity X in 4H-SiC. The bond distortions and atomic rattling near an impurity are incorporated, allowing optimization calculations to break free from the constraints of symmetry and gradually move towards
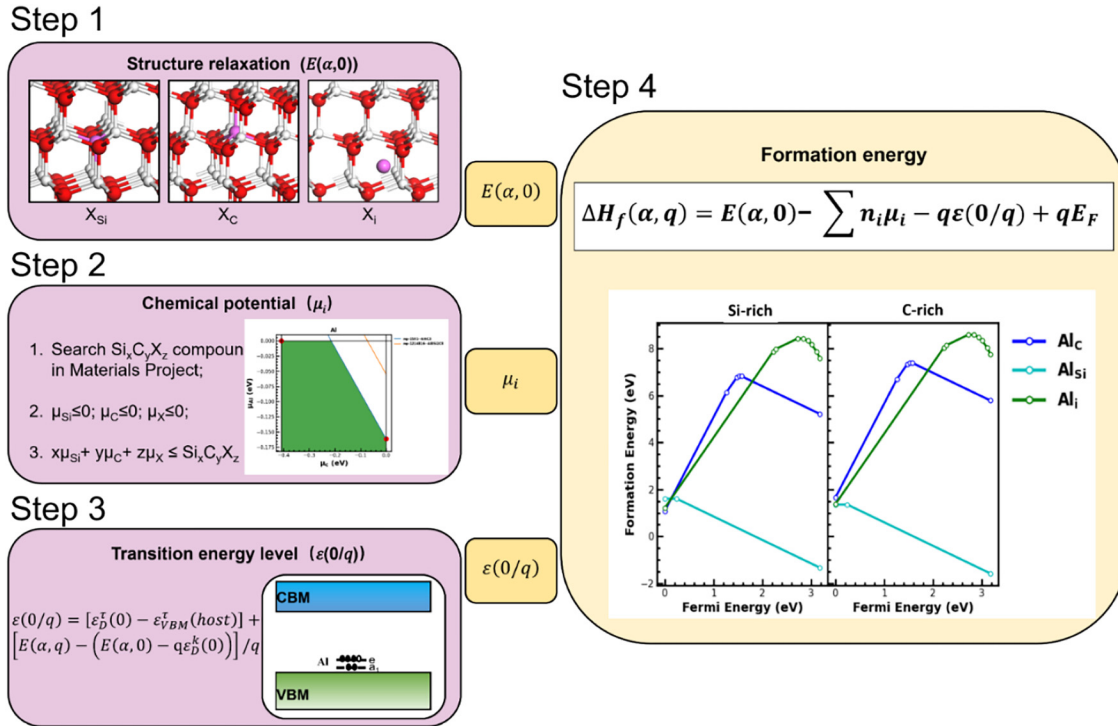
FIG. 1. Schematic workflow of the automated first-principles formation-energy calculations of impurity X in 4H-SiC. Step 1 is the generation of X_{Si}, X_C, and X_i configurations; step 2 is the determination of achievable values of μ_{Si}, μ_C, and μ_X; step 3 is the calculation of $\epsilon(0/q)$; step 4 is the formation energy $\Delta H_f(\alpha, q)$.

energetically favorable configurations. $E_{tot}(\alpha, 0)$ is obtained. For step 2, it is the determination of achievable values of μ_i. First, to avoid precipitation of the impurities and the host elements, μ_i are bound by

$$\mu_i \leq 0, \qquad (2)$$

Second, μ_i are limited to those values that maintain a stable host 4H-SiC,

$$\mu_{Si} + \mu_C = \Delta H_f(SiC), \qquad (3)$$

where $\Delta H_f(SiC)$ is the formation energy of host 4H-SiC. Finally, to avoid the formation of secondary phases between the impurities X and the host elements, μ_i is limited by

$$x\mu_{Si} + y\mu_C + z\mu_X \leq Si_xC_yX_z, \qquad (4)$$

In order to make the consideration of secondary compounds as complete as possible, the material genome database (Materials Project) is used to search for the competing secondary compounds.[48] Step 3 is the calculation of $\epsilon(0/q)$. To overcome the issue of a finite supercell size, $\epsilon(0/q)$ is calculated with the scheme by

using[7]

$$\epsilon(0/q) = [\varepsilon_D^\tau(0) - \varepsilon_{VBM}^\tau(host)]$$
$$+ [E_{tot}(\alpha, q) - (E_{tot}(\alpha, 0) - q\varepsilon_D^k(0))]/(-q) \qquad (5)$$

where $\varepsilon_D^\tau(0)$ and $\varepsilon_D^k(0)$ are the energies of the defect band at the Γ point and special k-point (weight averaged), respectively; $\varepsilon_{VBM}^\tau(host)$ is the VBM of the host at the Γ point; $E_{tot}(\alpha, q)$ is the total energy of the host supercell containing the defect α with the charge of q. The Freysoldt–Neugebauer–Van de Walle (FNV) correction is employed to alleviate spurious Coulomb interactions arising from finite-size supercells.[49] The first term on the right-hand side of Eq. (5) gives the single-electron defect level at the Γ point. The second term determines the U energy parameter (including both the Coulomb contribution and atomic relaxation contribution) of the charged defects calculated at the special k-points. Finally (step 4), the formation energy of $\Delta H_f(\alpha, q)$ can be obtained through Eq. (1). All the calculated formation-energy diagrams at Si- and C-rich limit are summarized in Part I of the supplementary material.

Based on the formation energies of impurities in 4H-SiC, a calculation using the detailed balance theory can be performed to determine the distribution of impurities as a function of temperature.[18] In this calculation, the formation of carbon vacancy (V_C) is

taken into consideration. V_C is identified as the dominant intrinsic defect in 4H-SiC, exhibiting the lowest formation energies among all intrinsic defects. Therefore, its presence and formation are considered in the calculation to accurately determine the impurity distribution with varying temperatures. The concentrations of holes and electrons are calculated by using

$$p_0 = N_v e^{(E_v - E_F)/k_B T} = N_v e^{-E_F/k_B T}, \quad (6)$$

$$n_0 = N_c e^{-(E_c - E_F)/k_B T} = N_c e^{(E_F - E_g)/k_B T}, \quad (7)$$

where E_v and E_c are the energies of VBM and conduction-band minimum (CBM) of 4H-SiC, respectively. E_v is usually set to zero. E_g is the bandgap of 4H-SiC. k_B is the Boltzmann constant. N_v and N_c are the effective densities of states of the valence bands and conduction bands, respectively. N_v and N_c are given by

$$N_v = 2(2\pi m_p^* k_B T)^{3/2}/h^3, \quad (8)$$

$$N_c = 2(2\pi m_n^* k_B T)^{3/2}/h^3, \quad (9)$$

where m_p^* and m_n^* are the effective mass of holes and electrons, respectively. Specifically, the effective masses for electrons and holes are taken as 0.42 and 1.75 m_0, respectively.[1] The charge neutrality condition requires that

$$p_0 + n_D^+ = n_0 + n_A^-, \quad (10)$$

where n_D^+ and n_A^- are the concentrations of positively charged donors and negatively charged acceptors, respectively. For ordinary doping conditions, the distribution of charged defects satisfies the Boltzmann distribution. Hence, the concentration for a defect α with charge state q is calculated by the Boltzmann distribution or

Fermi–Dirac distribution,

$$n(\alpha, q) = N_{\text{site}} g_q e^{-\Delta H_f(\alpha, q)/K_B T}, \quad (11)$$

where N_{site} is the number of sites that may be occupied by the defect α per volume, g_q is the degeneracy factor that corresponds to the number of possible electron configurations. By solving Eqs. (1) and (6)–(11) self-consistently, we can obtain the concentrations of impurities at a given temperature and chemical potential. The solubility (S_X) of an impurity (X) is the sum of all configurations at all possible charges, which can be expressed as

$$S_X = \sum_q n(X_{Si}, q) + \sum_q n(X_C, q) + \sum_q n(X_i, q). \quad (12)$$

III. RESULTS AND DISCUSSION

A. Site preference

Figure 2 illustrates the preferred sites of impurities in 4H-SiC based on the formation-energy diagrams discussed in Part I of the supplementary material. The figure provides information on the behavior of various impurities from different groups in the periodic table and their occupancy preferences at different Fermi energy levels. Group IA (excluding Li), group IIA, group IIIA (In and Tl), group VIIA, group VIII, group IB, and group IIB impurities: these impurities can occupy either the Si or C sites within a range of Fermi energies. They tend to occupy Si sites when the Fermi energy approaches the CBM. They occupy C sites when the Fermi energy approaches the VBM. Al and Ga of group IIIA, group IVA, group VA (excluding N), Te of group VIA, Y of group IIIB, and group IVB–VIIB impurities: these impurities predominantly occupy Si sites across the entire range of Fermi energies. N, Cl, Br, and group VI (excluding Te) impurities: these impurities preferentially occupy C sites in 4H-SiC. Sc and Y impurities: for n-type 4H-SiC, Sc and Y predominantly occupy Si sites. However, for
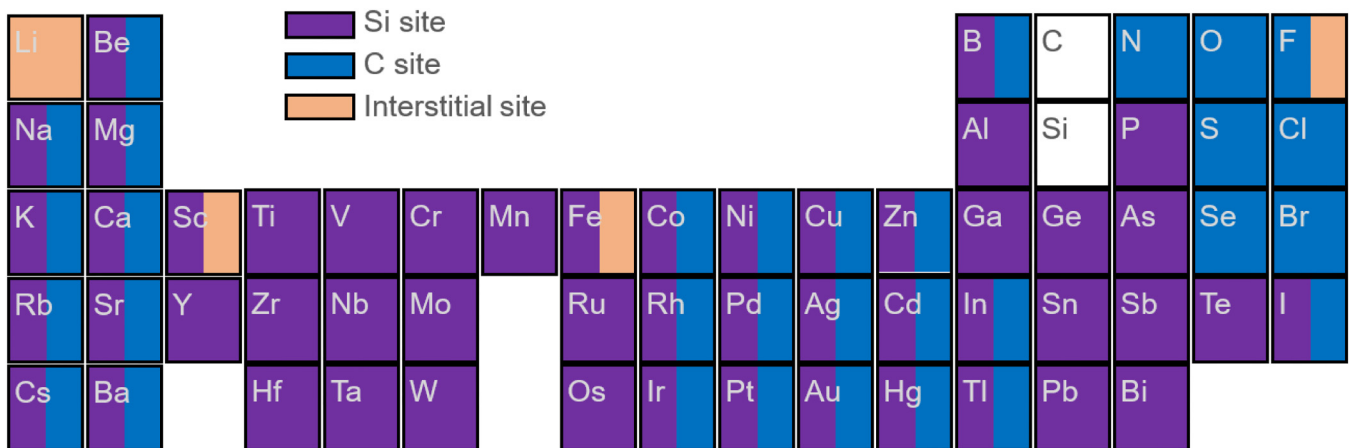

FIG. 2. Site preference of impurities in 4H-SiC. Purple, blue, and yellow represent the impurities occupying the Si site, C site, and interstitial site, respectively.

p-type 4H-SiC, they occupy interstitial sites. F impurity: for *n*-type 4H-SiC, F occupies the C site, while for *p*-type 4H-SiC, it occupies the interstitial site. The preferred site of B impurity is influenced by the chemical potential of Si or C. At the Si-rich limit, B occupies the C site, while at the C-rich limit, it occupies the Si site.

B. Lattice distortion

The impurity-induced lattice distortion in 4H-SiC is determined by the volume change $[(V-V_0)/V_0]$ before (V_0) and after doping (V). The lattice and atomic positions are allowed to relax during the structure relaxation process. As shown in Fig. 3 and Table S1 in the supplementary material, it is evident that the majority of impurities causes lattice expansion in 4H-SiC, while only B, N, and P result in lattice contraction. Specifically, when B occupies the Si site, it induces a lattice contraction of approximately −0.51%. N and P also create similar lattice contractions of around −0.15%. Excessive lattice distortion can have various effects, including phase transformation of 4H-SiC,[50,51] changes in wafer shape,[52] and the creation of intrinsic defects.[53,54] Co-doping with an expansion impurity and a contraction impurity is a common approach to address this issue. In the case of growing *p*-type 4H-SiC, a high doping concentration of Al (as high as $10^{19}\,cm^{-3}$) can lead to the formation of 6H-SiC inclusions. However, co-doping with Al-N or Al-B can effectively inhibit the formation of 6H-SiC inclusions.[50,51] Ge, Sn, and Pb are non-electroactive impurities in 4H-SiC, meaning that they do not directly impact the electrical characteristics of the material. As they have the same number of valence electrons as SiC, their substitution for Si does not create energy levels within the bandgap. However, co-doping Ge, Sn, or Pb with N can alleviate the stress induced by N-doping, thereby reducing the concentration of carbon vacancies in the material.

C. Solubility

The solubility of impurities in 4H-SiC, as a function of temperature ranging from 300 to 2400 K, is summarized in Part II of the supplementary material and Table S2 in the supplementary

material. The solubility data at 2400 K are particularly important because it corresponds to the normal growth temperature used in the commercial fabrication of single 4H-SiC crystals. The solubility of impurities in 4H-SiC is closely related to the atomic radius of the impurity element. Generally, if the difference in atomic radius between the impurity and the host Si or C is small, solubility tends to be high. Here are some key findings regarding the solubility of impurities in 4H-SiC at 2400 K, as depicted in Fig. 4. As for impurities in group IA, the solubility of Li is the highest, reaching approximately $10^{18}\,cm^{-3}$. The solubility of Na is around $10^{13}\,cm^{-3}$. However, K, Rb, and Cs have extremely low solubility and can hardly be doped into 4H-SiC. For group IIA, the solubility of Be is around $10^{18}\,cm^{-3}$, while the solubility of Mg is approximately $10^{17}\,cm^{-3}$. However, the solubility of Ca, Sr, and Ba is below $10^{13}\,cm^{-3}$. For group IIIA, the solubility of B, Al, and Ga is higher than $10^{19}\,cm^{-3}$. The solubility of In is around $10^{16}\,cm^{-3}$, and the solubility of Tl is approximately $10^{11}\,cm^{-3}$. Among these, Al has the highest solubility, reaching $3.3 \times 10^{20}\,cm^{-3}$ at the Si-rich limit and $4.3 \times 10^{20}\,cm^{-3}$ at the C-rich limit. For group IVA, the solubility of Ge is higher than $10^{19}\,cm^{-3}$, while the solubility of Sn is around $10^{16}\,cm^{-3}$, and the solubility of Pb is approximately $10^{11}\,cm^{-3}$. For group VIA, the solubility of N and P is higher than $10^{19}\,cm^{-3}$, while the solubility of As is around $10^{17}\,cm^{-3}$, and the solubility of Sb is approximately $10^{15}\,cm^{-3}$. The solubility of Bi is around $10^{11}\,cm^{-3}$. For both group VIA and group VIIA elements, the solubility is less than $10^{16}\,cm^{-3}$. For transition groups, the solubility of Sc, Ti, V, Mn, and Zn can exceed $10^{16}\,cm^{-3}$.

D. CTLs

Figure 5 shows the CTLs of impurities in 4H-SiC. Additional specific data on CTLs can be found in Table S3 in the supplementary material. According to the calculated CTLs of impurities in 4H-SiC, impurities can be categorized into four types based on their electronic behavior: *n*-type impurities, *p*-type impurities, amphoteric impurities, and non-electroactive impurities. Figure 6 provides a visual representation of the classification of
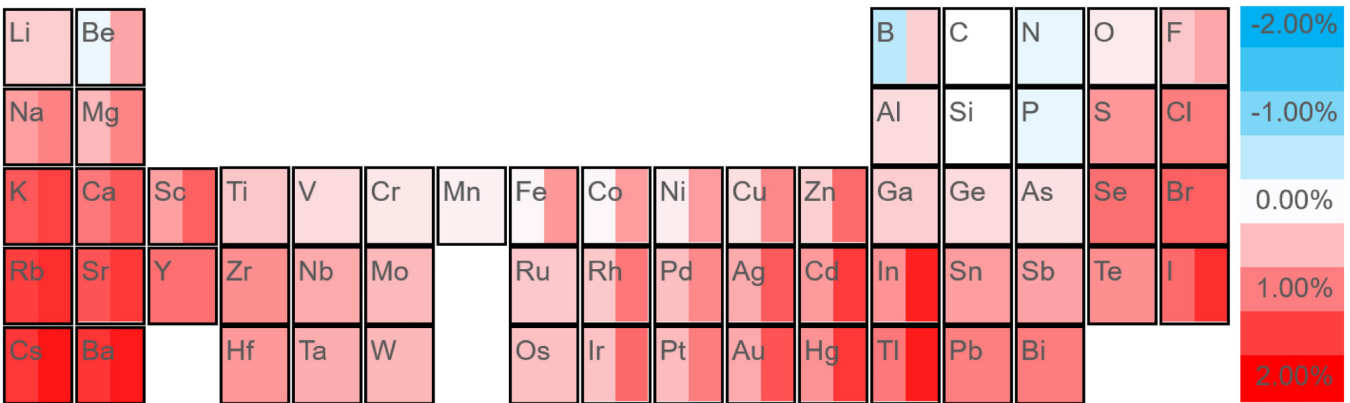

FIG. 3. Lattice distortion of 4H-SiC induced by impurity. The impurity-induced lattice distortion is determined by the volume change$((V - V_0)/V_0)$ after and before doping in 4H-SiC. Red (positive values) represents lattice expansion, while blue (negative values) represents lattice contraction.
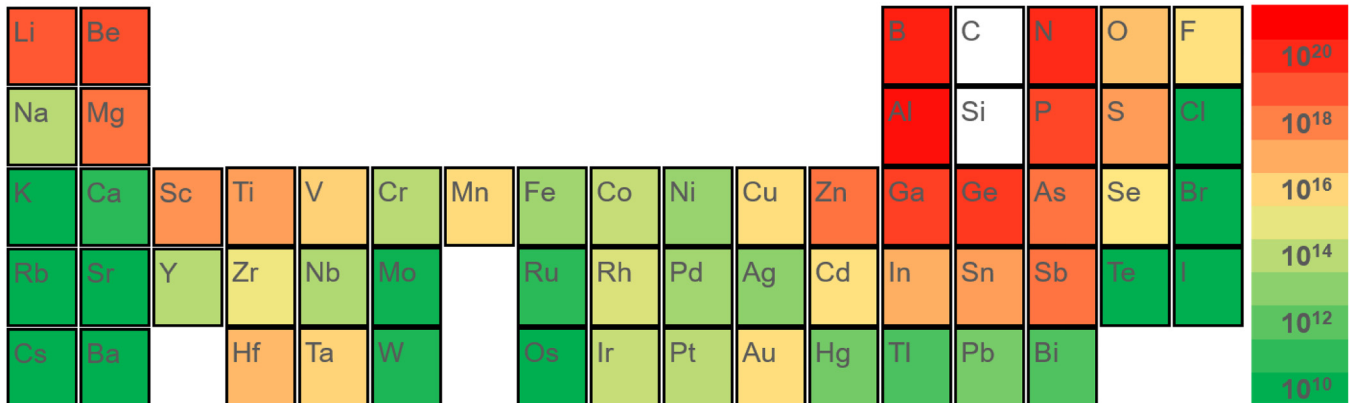
FIG. 4. The solubility of impurities in 4H-SiC at 2400 K. Solubility ranges from 10^{10} to 10^{21} cm^{-3} are denoted by a color gradient from green to yellow to red.

impurities into these four types based on their electronic behavior in 4H-SiC.

n-type impurities—Li, group VA and group VIA are the major *n*-type impurities in 4H-SiC. As for Li, Li mainly occupies the interstitial site of 4H-SiC. Li$_i$ creates a half occupied a_1 energy level closed to the CBM. The calculated $\varepsilon(0/1+)$ is $E_V + 2.97$ eV. As for other impurities of group IA, they mainly substitute on the Si or C site and create deep 1/4 occupied e energy levels. This results in their amphoteric characteristics. The impurities in group VA is the most often used *n*-type impurities due to the lower ionization energy and higher solubility.[12–16] N mainly substitutes on the C site and the calculated $\varepsilon(0/1+)$ of N_C is 0.06 eV (0.12 eV) for the hexagonal (cubic) site. P mainly substitutes on the Si site and the calculated $\varepsilon(0/1+)$ of P_{Si} is 0.06 eV (0.12 eV) for the h (k) site. For group VIA, O and S are deeper donors. O and S predominantly substitute on C sites. After substitution, they are able to donate two electrons. The calculated $\varepsilon(0/1+)$ and $\varepsilon(1+/2+)$ for O are $E_V + 1.95$ eV and $E_V + 1.58$ eV, respectively. The calculated $\varepsilon(0/1+)$ and $\varepsilon(1+/2+)$ for S are $E_V + 2.55$ eV and $E_V + 2.39$ eV, respectively. However, the solubility of O and S is so low that they are almost impossible to dope into 4H-SiC.

p-type impurities—group IIIA, group IIIB, and group-IVB are the major *p*-type impurities in 4H-SiC. For B, Al, Ga, and In in group IIIA are the well-known *p*-type impurities.[17–21] When they are substituted on the Si or C site, it will create a 3/4 occupied e energy level closed to the valance band. Among them, doping Al shows the highest doping efficiency due to the lowest ionization energy and highest solubility. Al mainly substitutes on the Si site, the calculated $\varepsilon(0/1-)$ of Al$_{Si}$ is at $E_V + 0.23$ eV. The solubility of Al can reach $\sim 10^{20}$ cm^{-3} as mentioned above. As for B, the doping behavior is highly related to the chemical potential of C. At the Si-rich limit, B mainly substitutes on the C site, B$_C$ creates $\varepsilon(0/1-)$ at $E_V + 0.44$ eV. At the C-rich limit, B mainly substitutes on the Si site, B$_{Si}$ creates $\varepsilon(0/1-)$ at $E_V + 0.27$ eV. B is rarely used for *p*-type doping because of its abnormal diffusion that would significantly affect the stability of the device. Ga and In exhibit higher ionization energy making them rarely used for *p*-type doping. For group IIIB,

they also have three valence electrons. After substituting on the Si site, Sc$_{Si}$ creates a $\varepsilon(0/1-)$ at $E_V + 0.22$ eV and Y$_{Si}$ creates a $\varepsilon(0/1-)$ at $E_V + 0.41$ eV. For group IVB, they have four valence electrons with the d^2s^2 arrangement. In the C$_{3v}$ symmetry of 4H-SiC, the d orbital splits into one full occupied a_1 state and two unoccupied e states. As the d orbital energy is lower than that of the p orbital of Si, the defect states are created from the host conduction-band states that move downward in energy, which contain one unoccupied a_1 state and two unoccupied e states. Ti$_{Si}$, Zr$_{Si}$, and Hf$_{Si}$ create a deep acceptor level $\varepsilon(0/1-)$ at $E_v + 3.06$ eV, $E_v + 3.12$ eV, and $E_v + 3.13$ eV, respectively.

Amphoteric impurities—group IA (excluding Li), group IIA, group VIIA, group VB-VIIB, and group VIII are the major amphoteric impurities. The doping behavior of H has been well studied in our previous work. We found that H_i^{bc} (interstitial H at the bonding center of the Si–C bond) and H_i^{Si-Te} (interstitial H at the tetrahedral center of Si) are the main configurations. H_i^{bc} creates a $\varepsilon(1+/1-)$ at $E_V + 2.80$ eV and H_i^{Si-te} creates a $\varepsilon(1+/1-)$ at $E_V + 0.34$ eV. For group IA (excluding Li), group IIA, I in group VIIA, group IB, group IIB, and group VIII, when they are substituted on the Si site they exhibit *p*-type characteristics and when they are substituted on the C site they exhibit *n*-type characteristics. V is often employed to compensate for the unintentional doping of N and B in order to produce the semi-insulating 4H-SiC.[28,29] V has five valence electrons. When V is substituted on the Si site, V$_{Si}$ creates a deep 1/2 occupied a_1 energy levels. The CTLs is $\varepsilon(0/1+)$ at $E_V + 0.91$ eV and $\varepsilon(0/1-)$ at $E_V + 1.90$ eV. For Cr, Cr substitutes on the Si site and Cr$_{Si}$ creates $\varepsilon(0/2+)$ at $E_V + 0.76$ eV, $\varepsilon(0/2-)$ at $E_V + 2.75$ eV and $\varepsilon(2-/3-)$ at $E_V + 3.12$ eV. For Mn, Mn substitutes on the Si site and Mn$_{Si}$ creates $\varepsilon(0/1+)$ at $E_V + 0.81$ eV and $\varepsilon(0/1-)$ at $E_V + 1.13$ eV.

Non-electroactive impurities—Ge, Sn, and Pb are non-electroactive impurities. Ge, Sn, and Pb have the same number valence electrons as Si/C. When Si is substituted, no energy levels are created within the bandgap.[32] It does not impact the electrical characteristics of 4H-SiC.
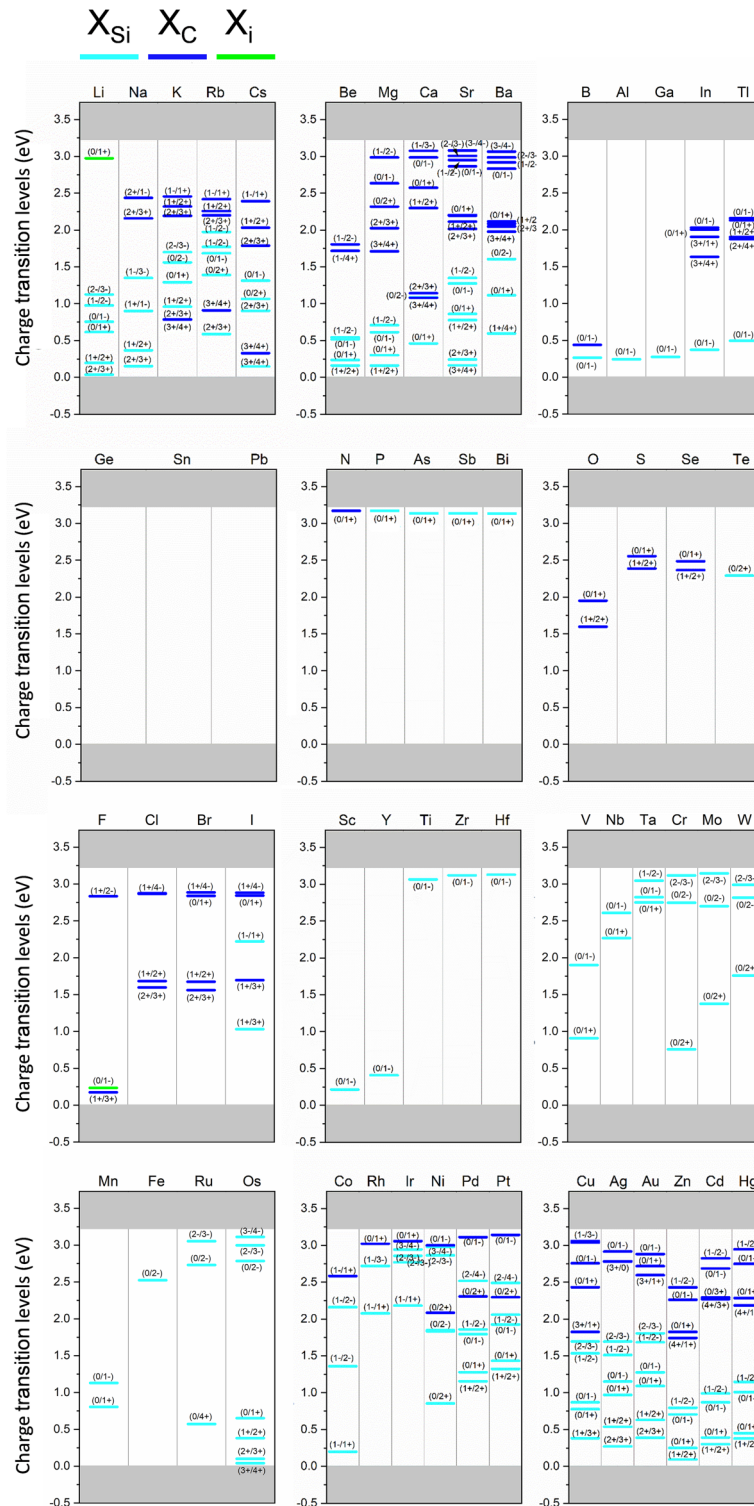
18 May 2024 05:50:52

FIG. 5. Charge transition levels of impurities in 4H-SiC. The sky blue, dark blue, and green bars represent charge transition levels where the impurity occupies Si, C, and interstitial sites, respectively.
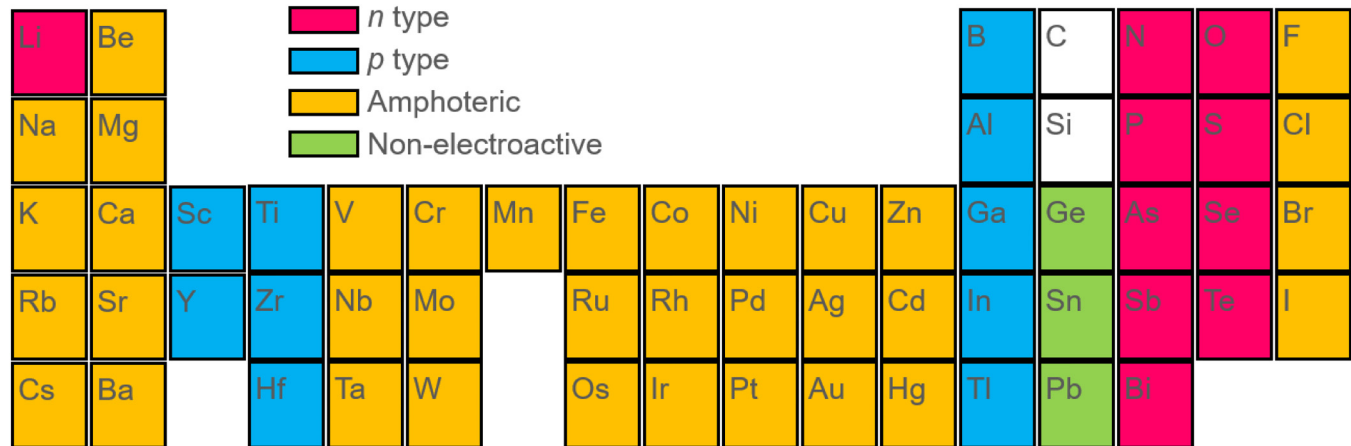
FIG. 6. Classifications of impurities in 4H-SiC: *n*-type impurities (red), *p*-type impurities (blue), amphoteric impurities (yellow), and non-electroactive impurities (green).

E. Perspective of doping in 4H-SiC

In high-power electronics applications, precise control of electronic conductivity through intentional doping is crucial for 4H-SiC. N-doping is the primary method used to achieve *n*-type conductivity in 4H-SiC. N-doping is accomplished by introducing nitrogen gas into the growth ambient during the fabrication process, typically using a mixture of Ar and N_2. The N density in the resulting 4H-SiC single crystal is approximately proportional to the square root of the nitrogen partial pressure during growth, and it is largely independent of the growth rate. Commercial *n*-type 4H-SiC wafers typically exhibit resistivities ranging from 0.015 to $0.025\,\Omega\,cm$, corresponding to a nitrogen impurity density range of 6×10^{18}–$1.5 \times 10^{19}\,cm^{-3}$. Recent advancements have significantly improved the specific on-resistance of 4H-SiC devices, reaching values as low as $1\,m\Omega\,cm^2$.[53] Consequently, the resistance of the 4H-SiC bulk substrate has emerged as a significant factor contributing to the overall resistance of the device. In conventional *n*-type 4H-SiC bulk substrates, the resistivity usually exceeds $10\,m\Omega\,cm$. However, simply adjusting process parameters is insufficient to overcome the doping concentration limit of N in 4H-SiC. Researchers such as Kato *et al.* have achieved an increase in N concentration to $1 \times 10^{20}\,cm^{-3}$ and a decrease in resistivity to $6.9\,m\Omega\,cm^2$ through the co-doping of Al-N.[55] This is because Al and N induce opposite lattice distortions: N-doping causes lattice contraction, while Al doping causes lattice expansion. Al-N co-doping enhances N-doping concentration. However, a major limitation of Al-N co-doping is the challenge of controlling the doping concentration of Al. If the Al doping concentration exceeds that of N, 4H-SiC will exhibit *p*-type conductivity instead. Considering this limitation, co-doping with Ge, as demonstrated in the aforementioned study, may be a more favorable alternative. Ge is a non-electrically active impurity that induces lattice expansion. Ge-N co-doping could potentially offer advantages in achieving low-resistivity *n*-type 4H-SiC, providing a promising avenue for further research and development.

In the field of ultra-high-power electronics for high voltage grids and high-speed trains, *p*-type 4H-SiC finds attractive applications. However, the development of *p*-type doping lags behind *n*-type doping in 4H-SiC. Among all group-III elements, Al has been found to be the best *p*-type impurity in 4H-SiC. The ionization energy of Al in 4H-SiC is 0.23 eV, which leads to incomplete ionization and limited doping efficiency of Al. The defect state of Al_{Si} originates from the VBM of 4H-SiC, which shifts upward in energy. The defect state is double degenerate (*e*-state) and occupied by three electrons. To push the defect state of Al_{Si} downward toward the VBM of 4H-SiC, a defect with an empty *e*-state is desired to ensure repulsion between these defect states with the same symmetry and the ability to accept electrons from the VBM of 4H-SiC. First-principles calculations suggest that group-IVB impurities, particularly Ti, are promising in reducing the ionization energy of Al_{Si}.

Caution should be exercised regarding unintentional doping. Due to the growth of 4H-SiC in a graphite system, it is difficult to avoid the incorporation of metal impurities from graphite into the single crystal of 4H-SiC. As mentioned above, the solid solubility of Sc, Ti, V, Mn, and Zn exceeds $1.0 \times 10^{16}\,cm^{-3}$, and they all act as deep-level defects. Unintentional doping of transition metals can significantly impact the carrier lifetime. Therefore, it is essential to ensure the purity of the graphite during the growth process.

IV. CONCLUSIONS

In this study, we have constructed a comprehensive database comprising formation-energy diagrams of impurities in 4H-SiC. Utilizing first-principles formation-energy calculations, we have included all impurities from the periodic table, with the exclusion of radioactive elements, rare earth elements, and group VIIIA elements. This database serves as a valuable resource for analyzing various aspects of impurities, such as site preference, lattice distortion, solubility, charge transition levels (CTLs), and electrical characteristics. The availability of this property database for impurities

18 May 2024 05:50:52

in 4H-SiC will greatly facilitate the engineering of material properties through doping strategies.

SUPPLEMENTARY MATERIAL

See the supplementary material for formation-energy diagrams of impurities (from Fig. S1 to Fig. S58); solubility of impurities as a function of temperature (from Fig. S59 to Fig. S114); Table S1 for lattice distortion of 4H-SiC induced by doping; Table S2 for the solubility of impurities in 4H-SiC at 300, 600, 1800, and 2400 K, and Table S3 for charge transition levels of impurities in 4H-SiC.

AUTHOR DECLARATIONS

Conflict of Interest

The authors declare no conflicts of interest.

Author Contributions

Yuanchao Huang: Data curation (equal); Investigation (equal); Methodology (equal); Software (equal); Writing – original draft (equal). **Rong Wang:** Methodology (equal); Supervision (equal); Writing – review & editing (equal). **Deren Yang:** Project administration (equal); Resources (equal); Supervision (equal). **Xiaodong Pi:** Funding acquisition (equal); Project administration (equal); Supervision (equal); Writing – review & editing (equal).

DATA AVAILABILITY

The data that support the findings of this study are available within the article and its supplementary material.

REFERENCES

[1] T. Kimoto and J. A. Cooper, *Fundamentals of Silicon Carbide Technology: Growth, Characterization, Devices and Applications* (John Wiley & Sons, 2014).

[2] J. B. Casady and R. W. Johnson, Solid State Electron. **39**, 1409 (1996).

[3] M. Bhatnagar and B. J. Baliga, IEEE Trans. Electron Devices **40**, 645 (1993).

[4] P. M. Fahey, P. B. Griffin, and J. D. Plummer, Rev. Mod. Phys. **61**, 289 (1989).

[5] C. G. Van de Walle and J. Neugebauer, J. Appl. Phys. **95**, 3851 (2004).

[6] A. Mannodi-Kanakkithodi, M. Y. Toriyama, F. G. Sen, M. J. Davis, R. F. Klie, and M. K. Y. Chan, NPJ Comput. Mater. **6**, 1 (2020).

[7] S. H. Wei, Comput. Mater. Sci. **30**, 337 (2004).

[8] K. Yim, J. Lee, D. Lee, M. Lee, E. Cho, H. S. Lee, H. H. Nahm, and S. Han, Sci. Rep. **7**, 1 (2017).

[9] C. Zimmermann, Y. K. Frodason, A. W. Barnard, J. B. Varley, K. Irmscher, Z. Galazka, A. Karjalaninen, W. E. Meyer, F. D. Auret, and L. Vines, Appl. Phys. Lett. **116**, 072101 (2020).

[10] H. Li, M. Huang, and S. Chen, J. Semicond. **41**, 032104 (2020).

[11] C. L. Yao, J. C. Li, W. Gao, A. Tkatchenko, and Q. Jiang, Phys. Rev. B **96**, 245203 (2017).

[12] U. Gerstmann, E. Rauls, T. Frauenheim, and H. Overhof, Phys. Rev. B **67**, 205202 (2003).

[13] K. Onoue, T. Nishikawa, M. Katsuno, N. Ohtani, H. Y. H. Yashiro, and M. K. M. Kanaya, J. Appl. Phys. **35**, 2240 (1996).

[14] G. A. Slack and R. I. Scace, J. Chem. Phys. **42**, 805 (1965).

[15] F. Roccaforte, P. Fiorenza, M. Vivona, G. Greco, and F. Giannazzo, Materials **14**, 3923 (2021).

[16] M. Bockstedte, A. Mattausch, and O. Pankratov, Appl. Phys. Lett. **85**, 58 (2004).

[17] Y. Huang, R. Wang, Y. Qian, Y. Zhang, D. Yang, and X. Pi, Chin. Phys. B **31**, 046104 (2022).

[18] Y. Huang, R. Wang, Y. Zhang, D. Yang, and X. Pi, J. Appl. Phys. **131**, 185703 (2022).

[19] Y. Huang, Y. Qian, Y. Zhang, D. Yang, and X. Pi, J. Appl. Phys. **132**, 015701 (2022).

[20] R. Wang, Y. Huang, D. Yang, and X. Pi, "Impurities and defects in 4H silicon carbide," Appl. Phys. Lett. **122**, 180501 (2023).

[21] Y. M. Tairov and Y. A. Vodakov, "*Topics in Applied Physics,*" in *Electroluminescence*, edited by J. I. Pankove (Springer-Verlag, Berlin, 1977), Vol. 7, p. 31.

[22] W. Suttrop, G. Pensl, and P. Lanig, Appl. Phys. A **51**, 231 (1990).

[23] Y. Gao, S. I. Soloviev, and T. S. Sudarshan, Appl. Phys. Lett. **83**, 905 (2003).

[24] H. Bracht, N. A. Stolwijk, M. Laube, and G. Pensl, Appl. Phys. Lett. **77**, 3188 (2000).

[25] M. A. Fanton, R. L. Cavalero, B. E. Weiland, R. G. Ray, D. W. Snyder, R. D. Gamble, and W. J. Everson, J. Cryst. Growth **287**, 363 (2006).

[26] J. R. Jenny, S. G. Müller, A. Powell, V. F. Tsvetkov, H. M. Hobgood, R. C. Glass, and C. H. Carter, J. Electron. Mater. **31**, 366 (2002).

[27] J. R. Jenny, D. P. Malta, S. G. Müller, A. R. Powell, V. F. Tsvetkov, H. M. Hobgood, and C. H. Carter, J. Electron. Mater. **32**, 432 (2003).

[28] N. Achtziger and W. Witthuhn, Phys. Rev. B **57**, 12181 (1998).

[29] M. Kunzer, H. D. Müller, and U. Kaufmann, Phys. Rev. B **48**, 10846 (1993).

[30] M. Bickermann, D. Hofmann, T. L. Straubinger, R. Weingärtner, P. J. Wellmann, and A. Winnacker, Appl. Surf. Sci. **184**, 84 (2001).

[31] Y. Huang, R. Wang, Y. Zhang, D. Yang, and X. Pi, Chin. Phys. B **31**, 056108 (2022).

[32] M. Krieger, M. Rühl, T. Sledziewski, G. Ellrott, T. Palm, H. B. Weber, and M. Bockstedte, Mater. Sci. Forum **858**, 301 (2016).

[33] T. Sledziewski, M. Vivona, K. Alassaad, P. Kwasnicki, R. Arvinte, S. Beljakowa, H. B. Weber, F. Giannazzo, H. Peyre, V. Souliere, T. Chassagne, M. Zielinski, S. Juillaguet, G. Ferro, F. Roccaforte, and M. Krieger, J. Appl. Phys. **120**, 205701 (2016).

[34] M. K. Linnarsson, U. Zimmermann, J. Wong-Leung, A. Schöner, M. S. Janson, C. Jagadish, and B. G. Svensson, Appl. Surf. Sci. **203**, 427 (2003).

[35] M. S. Miao and W. R. L. Lambrecht, Phys. Rev. B **74**, 235218 (2006).

[36] T. Dalibor, G. Pensl, N. Nordell, and A. Schöner, Phys. Rev. B **55**, 13618 (1997).

[37] G. Pasold, N. Achtziger, J. Grillenberger, and W. Witthuhn, Mater. Sci. Forum **353**, 471 (2001).

[38] V. J. B. Torres, I. Capan, and J. Coutinho, Phys. Rev. B **106**, 224112 (2022).

[39] T. T. Petrenko and T. L. Petrenko, Phys. Rev. B **93**, 165203 (2016).

[40] M. Miyata, Y. Higashiguchi, and Y. Hayafuji, J. Appl. Phys. **104**, 12 (2008).

[41] A. Gali, D. Heringer, P. Deák, Z. Hajnal, T. Frauenheim, R. P. Devaty, and W. J. Choyke, Phys. Rev. B **66**, 125208 (2002).

[42] G. Alfieri and T. Kimoto, J. Appl. Phys. **111**, 10 (2012).

[43] G. Kresse and J. Hafner, Phys. Rev. B **47**, 558 (1993).

[44] J. P. Perdew, K. Burke, and M. Ernzerhof, Phys. Rev. Lett. **77**, 3865 (1996).

[45] J. P. Perdew, K. Burke, and Y. Wang, Phys. Rev. B **54**, 16533 (1996).

[46] J. Heyd, G. E. Scuseria, and M. Ernzerhof, J. Chem. Phys. **118**, 8207 (2003).

[47] J. Paier, M. Marsman, K. Hummer, G. Kresse, I. C. Gerber, and J. G. Ángyán, J. Chem. Phys. **124**, 154709 (2006).

18 May 2024 05:50:52

[48]A. Jain, S. P. Ong, G. Hautier, W. Chen, W. D. Richards, S. Dacek, S. Cholia, D. Gunter, D. Skinner, G. Ceder, and K. A. Persson, APL Mater. **1**, 011002 (2013).

[49]C. Freysoldt, J. Neugebauer, and C. G. Van de Walle, Phys. Rev. Lett. **102**, 016402 (2009).

[50]K. Eto, H. Suo, T. Kato, and H. Okumura, J. Cryst. Growth **470**, 154 (2017).

[51]X. Xie, L. Sun, X. Chen, X. Yang, X. Hu, and X. Xu, Scr. Mater. **167**, 76 (2019).

[52]N. A. Mahadik, H. Das, S. Stoupin, R. E. Stahlbush, P. L. Bonanno, X. Xu, V. Rengarajan, and G. E. Ruland, Sci. Rep. **10**, 1 (2020).

[53]N. T. Son, X. T. Trinh, L. S. Løvlie, B. G. Svensson, K. Kawahara, J. Suda, T. Umeda, J. Isoya, T. Makino, T. Ohshima, and E. Janzén, Phys. Rev. Lett. **109**, 187603 (2012).

[54]T. Kimoto, Jpn. J. Appl. Phys. **54**, 040103 (2015).

[55]T. Kato, K. Eto, S. Takagi, T. Miura, Y. Urakami, H. Kondo, F. Hirose, and H. Okumura, Mater. Sci. Forum **778–780**, 47 (2014).

18 May 2024 05:50:52